

This is a pre print version of the following article:

The structure of ZrO₂ phases and devitrification processes in a Ca-Zr-Si-O-based glass ceramic: a combined a-XRD and XAS study / C., Meneghini; S., Mobilio; Lusvarghi, Luca; F., Bondioli; Ferrari, Anna Maria; Manfredini, Tiziano; Siligardi, Cristina. - In: JOURNAL OF APPLIED CRYSTALLOGRAPHY. - ISSN 0021-8898. - STAMPA. - 37:(2004), pp. 890-900. [10.1107/S0021889804022307]

Terms of use:

The terms and conditions for the reuse of this version of the manuscript are specified in the publishing policy. For all terms of use and more information see the publisher's website.

07/01/2026 11:31

Journal of
Applied
Crystallography
ISSN 0021-8898
Editor: **Gernot Kostorz**

The structure of ZrO₂ phases and devitrification processes in a Ca-Zr-Si-O based glass-ceramic: a combined A-XRD and XAS study

Meneghini Carlo, Mobilio Settimio, Bondioli Federica, Ferrari Anna Maria, Manfredini T. and Siligardi Cristina

CONFIDENTIAL – NOT TO BE REPRODUCED, QUOTED NOR SHOWN TO OTHERS

SCIENTIFIC MANUSCRIPT

For review only.

Category: *research papers*

Co-editor:

Dr J.L. Hodeau

Laboratoire de Cristallographie - CNRS, 25 Avenue des Martyrs, BP 166, F-38042 Grenoble CEDEX 09, France

Telephone: 33 4 76881142

Fax: 33 4 76881038

Email: hodeau@grenoble.cnrs.fr

Contact author:

Carlo Meneghini

Physics, Universita' di Roma Tre, Via della Vasca Navale, 84, Roma , Italy, I-00146, Italy

Telephone: +39 06 5517 7217

Fax: + 39 06 5579303

Email: meneghini@fis.uniroma3.it

international union of crystallography

referee's report

Journal: Journal of Applied Crystallography

Paper reference: hx5013

Title: The structure of ZrO_2 phases and devitrification processes in a Ca-Zr-Si-O based glass-ceramic: a combined A-XRD and XAS study

Author(s): Meneghini Carlo, Mobilio Settimio, Bondioli Federica, Ferrari Anna Maria, Manfredini T. and Siligardi Cristina

Please either fax this form or e-mail your comments to the Co-editor. If you cannot review this manuscript by the desired deadline, please contact the Co-editor immediately so that it can be sent to another referee. This form is provided for your convenience. If preferred, your report may be returned in any other format.

1. Is the manuscript worthy of publication?
 Yes, as it is _____;
 Yes, with minor revision _____;
 Yes, but with major revision _____;
 No, not at all _____
2. Is the work technically sound? _____
 Does the evidence presented justify the conclusions drawn? _____
 If not, please specify.
3. Is the presentation as efficient as possible? _____
 Can any material be omitted or deposited? _____
 Please specify.
4. Is the choice of journal correct? _____
 (Not relevant to conference proceedings.)
5. Have the requirements of *Notes for Authors* been met? _____
6. Is the Literature adequately cited? _____
7. Revisions to be made by the author.
 If it is necessary to continue on another sheet, please enclose an extra unsigned copy.

Signature

Date

The structure of ZrO_2 phases and devitrification processes in a Ca-Zr-Si-O based glass-ceramic: a combined A-XRD and XAS study

CARLO MENEGHINI,^{a,b*} S. MOBILIO,^a L. LUSVARGHI,^c F. BONDIOLI,^c A.

M. FERRARI,^c T. MANFREDINI^c AND C. SILIGARDI^c

^a*Dipartimento di Fisica Università di "Roma Tre" Via della vasca navale 84 I-00146 Roma Italy,* ^b*INFM-OGG c/o ESRF Grenoble, France,* and ^c*Dipartimento Ingegneria dei Materiali e per l'Ambiente, Via Vignolese 905, 41100 Modena, Italy.*

E-mail: meneghini@fis.nuiroma3.it

(Received 0 XXXXXXXX 0000; accepted 0 XXXXXXXX 0000)

Abstract

The structure of Zr atomic environment in a $\text{CaO-ZrO}_2\text{-SiO}_2$ glass-ceramic has been studied combining x-ray absorption spectroscopy (XAS), X-ray diffraction (XRD) and anomalous-XRD (a-XRD) techniques as a function of thermal treatments. The analysis of XRD patterns demonstrates that the devitrification process, as a function of thermal treatment, proceeds through the partial segregation of Zr-depleted phases (Wollastonite-like) and Zr-rich phases (Zr-oxides). The XAS and a-XRD measurements at the Zr K edge have been exploited to get a closer insight on the atomic structure around Zr ions. In the as quenched glass the Zr is 6-fold coordinated to Oxygen atoms in an amorphous environment rich of Ca and Si. Thermal treatment firstly ($T=1000 - 1050^\circ\text{C}$) determines the partial segregation of Zr in form of oxide which crystalline structure is that of tetragonal Zirconia (t-ZrO_2). Raising the temperature ($T=1100^\circ\text{C}$) provokes the formation of ZrO_2 crystallites in the monoclinic crystallographic phase (Baddeleyite: m-ZrO_2). The analysis of XAS data demonstrates that a considerable amount of Zr still remains in an amorphous Calcium-Silicate phase.

1. Introduction

Glass-ceramics are composite materials obtained from partial devitrification of a parent glass through a controlled heating treatment (Strnad, 1986). The evolution of the glass structure under thermal treatment proceeds through thermodynamically metastable phases toward a final material made of microcrystalline phases finely dispersed into amorphous phases. The processes occurring during the devitrification and the physical properties of a glass-ceramic material basically depend on the composition, thermal treatments as well as on a number of factors, such as nucleation and crystallization phenomena, and chemical nature of the elements (Weinberg, 1993). An accurate knowledge of metastable phases and intermediate structures evolving during the thermal treatments are essential for a deep understanding the physical-chemistry processes giving rise to the final glass-ceramic material.

One of the basic systems in glass ceramics technology belongs to the $\text{CaO-ZrO}_2\text{-SiO}_2$ (CZS) ternary system (Kordyuk & Gul'ko, 1962). The large interest in adding Zirconium oxide (ZrO_2) to CaO-SiO_2 glasses springs out from the general improvement of chemical, thermal and mechanical features of the final material. ZrO_2 addition, in fact, increases the density, enhances the viscosity and, in general, improves the mechanical and chemical resistance (Amoros *et al.*, 1994; Escardino *et al.*, 1996). The role of Si, acting as glass network former, and that of Ca, acting as stabilizer network modifier, are well established. On the contrary the role of Zr, classified as intermediate between network former and modifier, is poorly understood. Adding ZrO_2 can have, in fact, different effects on the formation and development of the microcrystalline structure of the glass (Mac Millan, 1964; Neilson, 1972; Vogel, 1994): it can favour a metastable liquid-liquid phase separation with subsequent formation of crystalline nuclei in the phase separated regions; or it may form small crystallites acting as heterogeneous nucleation sites for the crystallization of the glass matrix.

The main purpose of this work is studying the atomic environment of Zr in a CZS glass-ceramic: $(\text{CaO})_x(\text{ZrO}_2)_y(\text{SiO}_2)_z$ ($x \sim 0.4$, $y \sim 0.05$, $z \sim 0.55$) as a function of thermal treatment. To this aim we exploited the ample complementarities of X-ray absorption spectroscopy (XAS) and anomalous X-ray Diffraction (a-XRD) techniques to probe atomic order around Zr ions at local, medium and long range scale. In particular we used XAS techniques, namely EXAFS (x-ray absorption fine structure) and XANES (x-ray absorption near edge structure), in order to probe the local atomic environment around the Zr, while we exploited the long-range order sensibility of a-XRD to probe the crystalline nature of the phases containing Zr.

Our results put in evidence the nucleation and growth of crystalline ZrO_2 phases from an amorphous Zirconium-Calcium Silicate (Si-Ca-Zr-O) phase, as a function of thermal treatment. The segregation of Zr-oxide particles proceed firstly with the formation of small t- ZrO_2 crystallites. Raising the temperature produces m- ZrO_2 crystallites. We observe that tetragonal ZrO_2 phase present systematically broader diffraction lines with respect to the monoclinic m- ZrO_2 phase (Beddeleyte structure) suggesting the presence of more defective/smaller crystallites in the t- ZrO_2 phase. The analysis of the XAS data shows that a considerable amount of Zr remains in the amorphous calcium silicate phase, even after firing the sample at 1100 °C.

2. Experimental

2.1. sample preparation and characterization

The studied glass belongs to the Wollastonite stability field of ternary $\text{CaO-ZrO}_2\text{-SiO}_2$ system (Matsumoto *et al.*, 1954). A mixture containing Calcium Carbonate (CaCO_3 100%), Silica (SiO_2 99.9 %) and Zirconium Silicate (ZrSiO_4 99.9%) as raw materials was prepared with weight ratios $\text{SiO}_2/\text{CaO} = 3/2$, and $\text{ZrO}_2=10$ wt%. The resulting molar composition of the sample was: $(\text{CaO})_{39.78}(\text{ZrO}_2)_{4.52}(\text{SiO}_2)_{55.70}$.

The mixture was melted in platinum crucible in an electric furnace at about 1590 °C for 40 minutes soaking time. The melted batch was quenched in a graphite crucible to obtain bar shaped pieces of glass. Plates of glass, 1 mm thick, were cut from the bars and thermally treated on a muffle kiln in order to obtain glass-ceramic materials. Samples were heated at 10 °C min⁻¹ to the T_a = 1000, 1050 and 1100 °C and were kept at T_a for 60 min, thus were placed on refractory bricks and slowly cooled down to room temperature (RT). None of the samples fractured during cooling. In the following we will refer to the as quenched (AQ) glass and treated samples as AQ, 1000, 1050 and 1100 respectively.

Samples were preliminary characterized by standard differential thermal analysis (DTA), electron microscopy (SEM) and standard X-ray diffraction techniques. DTA analysis was performed on about 30 mg of fine powders (grain size of about 20 μ m) placed in Pt crucible. DTA curves display a change in the sample specific heat due to a glass transition at T_g = 763°C, and an exothermic peak corresponding to a crystallization temperature at T_c = 969°C. SEM observations were performed on superficially polished gold-coated specimens. SEM images show, in all the fired samples, a poly-crystalline habit typical of Wollastonite. The sample treated at 1100 °C presents dispersed micrometer sized agglomerates of particles that appear white in backscattered electron analysis (figure 1) and must be attributed to Zr rich phases. Preliminary XRD characterization was achieved on a laboratory powder diffractometer (Philips PW3710) using a Ni filtered Cu-K α x-ray beam. In the as quenched glass the XRD patterns demonstrate the amorphous nature of the material while XRD patterns of fired samples depict the progressive evolution of crystalline phases as a function of temperature. Qualitative pattern analysis has showed that the principal crystalline phases developing during the thermal treatments are Wollastonite-like (CaSiO₃) but the samples treated at the higher temperature (1100 °C) demonstrate also the presence

of Baddeleyite (m-ZrO₂) phase.

2.2. Synchrotron radiation x-ray diffraction

Synchrotron radiation XRD patterns were collected at the GILDA (General Italian Line for Diffraction and Absorption) beamline (Pascarelli *et al.*, 1996) at the ESRF (European Synchrotron Radiation Facility), using an angle dispersed set-up based on an Imaging Plate (IP) detector (Meneghini *et al.*, 2001). Beam energies were selected using a double crystal (Si [311]), sagittal focusing, monochromator. An air filled ionization chamber monitored the incoming x-ray intensity that was kept constant by an active feedback system (PID feedback). The x-ray spot size on the sample was about $0.7(v) \times 1.5(h)$ mm², the horizontal dimension being limited by the sagittal focusing monochromator geometry, while the vertical size was selected in order to fully embed the capillary sample holder (see below). Beam energies were calibrated taking as reference point the first inflection point of the K-edge absorption coefficient of pure Zr metal foil (17998 eV). Samples for XRD were finely milled and enclosed in boro-silicate glass capillaries (inner diameter 0.5 mm). Capillaries were mounted on a goniometer head and kept rotating during data collection in order to improve the grain statistics. The geometrical parameters, namely the sample to IP distance, IP to x-ray beam perpendicularity and instrumental line broadening were calibrated collecting diffraction patterns of a LaB₆ standard reference material (NIST). The IP was digitised using a FUJI-BAS2500 reader with a pixel resolution of $100 \times 100 \mu m^2$ and a dynamical range of 10^6 counts/pixel. Digitised images were treated and integrated to a standard Intensity *vs* 2θ pattern using the Fit2D software (Hammersley *et al.*, 1994).

The angle dispersed set-up allows collecting diffraction patterns having very high count statistics keeping the collection time in the minute range. This allows detecting very fine details in the diffraction patterns (figure 4) and is mandatory for accurate

a-XRD experiments. In this study the only disadvantage of this set-up with respect to a 2θ scan geometry, is the reduced angular range ($2\theta_{max}$ is limited to 40-50 deg.) that shortens the available reciprocal space to a maximum exchanged momentum of $q_{max} \sim 6\text{\AA}^{-1}$. This drawback prevents an analysis of XRD and a-XRD in terms of radial distribution functions as done in our previous work (Meneghini *et al.*, 1999). The sample to detector distance and the sample holder diameter determine the instrumental line broadening (Meneghini *et al.*, 2001) that is $\Delta 2\theta_{instr} \sim 5 \times 10^{-2}$ deg. (FWHM), well below the minimum line width observed in our samples (~ 1.2 deg. in 110 sample) but quite large if compared with the intrinsic line width of a high resolution diffractometer. The various structural contributions to the line broadening (*i.e.* crystallite size, lattice defects, lattice strain) are different functions of the scattering angle (Warren, 1990), so that, at least in principle, it should be possible to distinguish between these effects and several methods have been developed to this end (Warren & Averbach, 1950; Warren & Averbach, 1952; Willilamson & Hall, 1953; Wilson, 1962). However the IP instrumental line broadening, coupled with the poor crystallographic nature of our glass-ceramics limit the applicability of these methods preventing for a complete line shape analysis. In particular strain- and size-related line broadening effects cannot be distinguished within this set-up. Thus we decided to assume, for shake of simplicity, the systematic evolution of ZrO_2 diffraction patterns as a function of thermal treatments, only related to a particle size effect. In this way the crystallite size reported in table 1 represent, instead, an upper limit to the true crystallite sizes.

Two series of XRD patterns were collected with beam energy at $E_1 = 17000$ eV ($\lambda = 0.7293$ Å), far below the Zr K edge, and $E_2 = 17990$ eV ($\lambda = 0.6892$ Å), near below the Zr K edge. A third series of XRD patterns was collected at $E_3 = 11846$ eV ($\lambda = 1.045$ Å), allowing for a closer insight on the crystallographic phases other than Zr-ones. Collection time was fixed to 3 minutes for each pattern. Raw XRD patterns

(E_3 series) of the four samples investigated are shown in figure 3: the XRD patterns of AQ sample present smooth and broad features typical of amorphous structures. The high quality of the data, however, reveals weak diffraction lines pointing out a negligible contribution of crystalline phases, remnants of the vitrification processes. Thermal treatment provokes the structural evolution involving the progressive growth of crystalline phases. Notice that the sample treated at 1050 °C presents evident changes also in the amorphous background suggesting that the firing process also modifies the structure of the glassy phases.

The so called anomalous (or resonant) scattering effect consists in a relative ample variation of the dispersion corrections (f' and f'') to the atomic scattering factor (f_o) of an element, in the energy region near an absorption edge (Materlik *et al.*, 1994). The anomalous-XRD technique exploits this effect to enhance the chemical selectivity toward the absorbing atomic species. The intensity of a Bragg diffraction peak is determined by the structure factor $S_{hkl}(q)$ that, in turn, is proportional to the atomic scattering factor of the ions involved. Tuning the x-ray beam energy near a specific absorption edge in the sample affects the intensity of those diffraction lines which structure factor involve that absorbing atomic specie. Thus the difference between XRD patterns collected tuning the beam energy far below (E_1) and near (E_2) a specific absorption edge in the sample retains only those structural features involving the absorbing atomic species (figure 4). In practice difference patterns are calculated as:

$$\Delta I(q) = I_{E_1}(q) - A(I_{E_2}(q) - B) \quad (1)$$

where $q = 4\pi \sin(\theta)/\lambda$. A and B are empirical parameters: A takes into account differences in beam intensity, IP sensitivity and x-ray absorption at the two energies; B reproduces the increasing fluorescence contribution near the Zr absorption edge. The A and B are determined minimizing the difference $\Delta I(q)$ in selected q-regions

regions of the diffraction patterns. Since Ca, Si and O ions present negligible dispersion in the used energy range used (see below), the contributions of Zr free phases are expected to disappear in the difference pattern ¹. The anomalous scattering factor variations (Dejus & del Rio, 1996) for Zr are $\Delta f'_{Zr} = f'(E_1) - f'(E_2) \sim 5.5$ and $\Delta f''_{Zr} = f''(E_1) - f''(E_2) \sim -0.95$. For the other ions the differences are much smaller (negligible): $\Delta f'_i < 1 \times 10^{-2}$ (i=Si, Ca, O); $\Delta f''_{Si,O} < 1 \times 10^{-2}$; $\Delta f''_{Ca} \sim 0.03$. Difference patterns are reported in figure 5. The difference pattern of the as quenched sample does not show diffraction lines meaning that the Zr is completely melted into the amorphous matrix. The difference pattern for 1000 sample depicts a weak but evident set of reflections closely resembling the diffraction pattern expected for t-ZrO₂ while new reflections, associated to the m-ZrO₂ phase, appear raising the firing temperature and became dominant in 1100 sample.

2.3. X-ray absorption spectroscopy

XAS experiments were carried out at the BM29 beamline (Filipponi *et al.*, 2000) at the European Synchrotron Radiation Facility (ESRF) in Grenoble (France). Beam energies were defined using a Si[111] double crystal - fixed exit monochromator. Harmonic rejection was achieved by detuning the monochromator crystals to 1/3 of the rocking curve. The monochromator crystal detuning and the large energy of the first allowed harmonic (> 50 keV) with respect to the ESRF critical energy (20 keV) ensure a high quality monochromatic beam with negligible harmonic content.

XAS spectra at the Zr K-edge (17998 eV) have been collected in standard transmission geometry with fixed $\delta k \simeq 0.024 \text{\AA}^{-1}$, leading to more than 10^3 points per

¹ Notice that the angle dispersed set-up prevents employing a data normalization and correction strategy suitable for parallel-beam high-resolution diffractometer (as for example the one proposed by Burger and coworkers (Burger *et al.*, 1988)). In our case, in fact, data normalization must take into account for air scattering and fluorescence background, detector efficiency, geometrical corrections and other factors which are difficult to precisely parameterize. On the contrary we found that all these effect can be simply and reliably taken into account by the A and B parameters

spectrum. Incident (I_o) and transmitted (I_t) x-ray intensities were measured using Ar filled ionization chambers. The absorption signal is defined as $\mu(E) = \ln(I_o/I_t)$. Fine samples powders were mixed with BN powders (1:5 weight ratio) and pressed in pellets. In order to reduce the effects of thermal disorder, that attenuate the structural EXAFS signal, samples were mounted in a closed-cycle He refrigerator and cooled down to about 30 K for data acquisition. The low signal to noise ratio² ($\sim 10^{-4}$) and the wide energy range extending up to about 2 keV above the edge (allowing to reach a maximum k (see below) higher than 18\AA^{-1}), ensure the high XAS data quality. The fig. 2 reports the raw absorption data for the four samples investigated.

The structural XAS signal, known as XAFS (X-ray Absorption Fine Structure), is defined as the relative oscillation of the absorption coefficient $\mu(k)$ around the atomic cross section $\mu_o(k)$, normalized to the atomic K-edge cross section (Lee & Pendry, 1975; Lee *et al.*, 1981):

$$\chi(k) = \frac{\mu(k) - \mu_o(k)}{\mu_o(k)}$$

where $k = \sqrt{2m(E - E_o)/\hbar^2}$ is the modulus of the photoelectron wave vector.

For a given distribution of neighbouring ions around the absorber a , *i.e.* for a given partial pair distribution function $4\pi\rho_or^2g_{ai}^{(2)}(r)$, the structural XAFS signal is written as (Filipponi *et al.*, 1995):

$$\chi_i(k) = \int_0^\infty 4\pi\rho_or^2g_{ai}^{(2)}(r)\gamma_{a,i}^{(2)}(k,r)dr \quad (2)$$

where the $\gamma_{a,i}^{(2)}(k,r)$ represents the contribution to the XAFS signal associated to a single ion i at a distance r from the absorber. In case of Gaussian distribution of

² The statistical noise of XAS data has been evaluated as follow: the post-edge $\mu(E)$ was fitted with high order polynomials simulating the structural signal. The statistical noise was then estimated as the variance of the difference, normalized to the jump eight, between polynomial functions and the experimental $\mu(E)$

neighbour shells the integration of eq. 2 gives rise to the well known formula (Lee *et al.*, 1981):

$$\chi_i(k) = A_{ai}(k) \frac{N_i}{kR_i^2} \sin(2kR_i + \phi_{ai}(k)) e^{-2k^2\sigma_i^2} e^{-2R_i/\lambda(k)} \quad (3)$$

and the total EXAFS signal is: $\chi(k) = S_o^2 \sum_i \chi_i(k)$. N_i is the coordination number, R_i the average shell radius and σ_i^2 the variance of the distribution. The A_{ai} and ϕ_{ai} are the amplitude and phase functions in the photoelectron backscattering process. S_o^2 is an empirical parameters taking into account many body losses and $\lambda(k)$ is the photoelectron mean free path.

Differently from x-ray scattering, the strong interaction of the photoelectron with the atomic potentials surrounding the absorber makes the XAS technique sensitive to the many body distribution functions (Lee *et al.*, 1981; Benfatto *et al.*, 1986; Filipponi *et al.*, 1995; Filipponi & Di Cicco, 1995). In the so called EXAFS (extended x-ray absorption spectroscopy) region, that starts some tenth of eV above the edge, the limited (few Å) photoelectron mean free path, the $1/R_i^2$ and the Debye-Waller terms suppress the contribution coming from long photoelectron paths, so that the multiple scattering and/or medium range order effects are generally weak. In the near edge region (XANES) the multiple scattering effects are dominant, making the XANES highly sensitive to the topology of the atomic environment (Lee *et al.*, 1981; Benfatto *et al.*, 1986). In addition the details of the electronic configuration near the Fermi level are also relevant in the XANES region. The large amount of information (structural and electronic) makes an ab-initio quantitative interpretation of the XANES region a difficult task. Nevertheless relevant information can be still obtained empirically, comparing the experimental data with reference materials and/or simulations. (Bianconi, 1988)

The XANES region has been interpreted with the help of simulated spectra cal-

culated using the FEFF8.0 package (Ankudinov *et al.*, 1998). The analysis of the EXAFS data was performed using the GNXAS package (Filipponi *et al.*, 1995; Filipponi & Di Cicco, 1995) along the lines already described in a previous work (Meneghini *et al.*, 1999).

3. Results and discussion

3.1. XRD.

The XRD patterns reported in figure 3 depict the progressive devitrification process as a function of the heating temperature. In the as quenched glass weak Bragg reflections point out the presence of weak amount of crystalline phases (estimated lower than 1%) that survived to the vitrification process. These contributions were not detected by a previous laboratory XRD analysis. In particular the most intense peak at about 17.73 deg. corresponds to the (101) reflection ($d=3.39$ Å) of quartz (SiO_2) (Wright & Lehmann, 1981). A similar contribution has been observed in previous work (Meneghini *et al.*, 1999), however the much better statistics in these patterns allows now a more reliable peak assignment. This is evident looking at the middle panel in figure 3 which reports the XRD pattern of AQ sample subtracted of the background (simulated with a smooth polynomial). The features corresponding to the Quartz phase are clearly recognized, while contributions of other crystalline phases can be excluded.

In 1000, 1050 and 1100 samples XRD patterns of crystalline phases became evident (figure 3). Even if the main reflections can be indexed within a Wollastonite-like structures (see for example the lower panel in figure 3), the pattern appears really complex and several crystalline unknown phases are involved so that the quantitative interpretation of the whole XRD patterns as a function of thermal treatment is a difficult task which would give poorly reliable results. In the present study we principally focus on

the Zr-containing phases; therefore we exploited the a-XRD technique at the Zr K-edge. The difference patterns reported in figure 5 demonstrate that the Zr-containing phases evolve as a function of thermal treatment: the difference pattern of 1000 sample presents a weak but visible family of peaks closely resembling the pattern expected in t-ZrO₂. Notice that cubic (c-ZrO₂) tetragonal (t-ZrO₂) Zirconia phases have very similar XRD patterns, the main difference being the splitting of some reflections due to the reduced symmetry of tetragonal phase. The broad diffraction lines observed in the difference pattern of 1000 sample does not allow distinguishing between cubic and tetragonal phases. However a sizable amount of cubic Zirconia can be excluded on the basis of XANES results (see below). This finding demonstrates the early nucleation of ZrO₂ tetragonal phase that, owing its weakness, we did not see in our previous works. In the difference pattern of 1050 sample a new set of reflection appears. These new reflections are readily associated to the m-ZrO₂ phase. In the sample 1100 the contribution of m-ZrO₂ phase increases with respect to the t-ZrO₂ one and becomes dominant.

In order to have quantitative information, the difference patterns were refined within the Rietveld full profile refinement approach (GSAS package (Larsen & Von Dreele, 2000)) using a pseudo-Voigt profile function. The t-ZrO₂ phase contribution has been refined within the P42/nmc space group (N. 137) (Canton *et al.*, 1999). The atomic positions where Zr (0.75, 0.25, 0.25) and O (0.25, 0.25, 0.450). The m-ZrO₂ phase contribution has been refined within the P21/c space group (N. 14) (Hann & Al, 1985). The atomic positions were kept fixed at Zr (0.274, 0.039, 0.209), O₁ (0.063, 0.328, 0.347) and O₂ (0.449, 0.755, 0.482). The results of Rietveld analysis are reported in table 1. The refined unit cell of tetragonal phase has $a = 3.63\text{\AA}$, in good agreement with the value $a = 3.629\text{\AA}$ expected for pure t-ZrO₂ (Canton *et al.*, 1999), but the cell appears slightly elongated along c ($c = 5.23\text{\AA}$) with respect to the pure t-ZrO₂

in which $c = 5.197\text{\AA}$. The b and c cell edges refined for the monoclinic phase appear slightly enlarged ($\sim 1\%$) with respect to the reference m-ZrO₂ (Hann & Al, 1985) structure.

The tetragonal phase presents diffraction lines systematically broader than those of the monoclinic phase. Crystallite size, lattice defects and strain concur to enlarge the diffraction lines, then this trend suggests that the tetragonal phase is made of more poorly crystallized (smaller and/or more defective) particles with respect to the monoclinic phase. Owing the aforementioned limitation of the IP based set-up, only the particle size was estimated by the line profile analysis applying the Sherrer formula as described in the GSAS manual: $D(\text{\AA}) = K\lambda/L_x$, where L_x is the Lorentzian contribution to the line shape and $K=0.9$ is the Sherrer constant. Standing these approximations, the maximum particle size in t-ZrO₂ phase is about 80 Å in sample treated at 1000 °C, and increases to about 150 Å after firing at 1050 °C and 1100 °C. On the contrary the maximum size of m-ZrO₂ crystallites is sensibly larger being about 200 Å in 1050 sample and growing up to about 400 Å in 1100 sample. The relative volume fraction for m-ZrO₂ and t-ZrO₂ phases are reported in the last column of table 1 and demonstrate the progressive evolution of ZrO₂ phases from tetragonal to monoclinic. The appearance of metastable t-ZrO₂ in form of small particles in samples treated at lower temperatures must be related to the peculiar particle size dependent phase diagram (Garvie, 1965) of ZrO₂ which shows that reducing the particle size enhances the stability of t-ZrO₂ phase over the m-ZrO₂ one. It has been demonstrated that this peculiar trend originates from the considerably larger surface energy in m-ZrO₂ with respect t-ZrO₂ phase. Thus increasing the surface to volume ratio raises the molar free energy of m-ZrO₂ making the t-ZrO₂ energetically more favourable. Thermodynamic calculations (Garvie, 1978) estimated the critical size for t-ZrO₂ phase stability around 100-120 Å. This value is in good agreement with the

upper limit for t-ZrO₂ crystallites we have found around 150Å.

The most relevant information derived from a-XRD are that the temperature treatment provokes the crystallization of ZrO₂ oxide phases: firstly tetragonal, then monoclinic. In addition a-XRD results exclude the growth of crystalline phases containing Zr different from ZrO₂.

3.2. X-ray Absorption Spectroscopy

The analysis of the XAS spectra concerns both the extended and the near edge regions. In the XANES region the available information mainly derives from a qualitative or semi-quantitative comparison with available models. The analysis of the EXAFS spectra, that was performed taking into account a-XRD and XANES results, allowed a more quantitative insight on the average local structure around Zr.

3.2.1. XANES. The sensibility of the XANES region of the absorption spectra to the topology of the local atomic environment around the absorber, will help in definitively assess the local atomic structure around Zr this CZS glass ceramic as a function of thermal treatment.

The experimental XANES data for the four investigated samples are shown in figure 6 in which we also show the theoretical XANES calculated on the basis of crystallographic Zr polytypes: c-ZrO₂ (Li *et al.*, 1993), t-ZrO₂ (Canton *et al.*, 1999), m-ZrO₂ (Hann & Al, 1985) (baddeleyite) and CaZrSi₂O₇ (Roelofsen-Ahl & Peterson, 1989) (Gittinsite). The Gittinsite model has been choose after several tests on different Ca-Zr silicates as the one giving the best agreement between theoretical and calculated XANES. The local atomic environments of the four models are shown in figure 9. In all the samples preliminary refinements have shown a negligible fraction of c-ZrO₂ allow excluding a cubic environment for Zr in these samples.

The experimental XANES change weakly between AQ and 1000 samples. This trend is rather different from what observed in XRD patterns of AQ and 1000 samples in which the crystallization progress is well evident. In agreement with our previous results (Meneghini *et al.*, 1999), this finding suggests that the early stages of devitrification process have only minor effect on the Zr local environment, mainly affecting the Wollastonite-like phases. Raising the firing temperature (1050 and 1100 samples) provokes large modifications also in the Zr environment.

The experimental XANES data of AQ and 1000 samples present two main features (labelled as *a* and *b* in figure 6). These features closely resemble those found in Gittinsite and suggest an octahedral arrangement of Oxygen neighbours around Zr. In 1050 sample a new contribution (labelled as *c* in figure 6) appears between the *a* and *b* shoulders, this peak is close the single maximum found in the XANES calculated for t-ZrO₂ and m-ZrO₂ structures. The XANES features of 1100 sample definitively evolve closely to the curves calculated for m-ZrO₂ model. In order to get a quantitative interpretation of the XANES region we fitted the experimental data with a linear combination of the three models: m-ZrO₂, t-ZrO₂, and Gittinsite. The fitting demonstrates that in the AQ sample the 80% of Zr is embedded in a calcium silicate glassy phase whose local structure closely resembles that of Gittinsite. Even in the AQ sample about 20% of Zr has a local environment similar to that of t-ZrO₂. Both these phases must be amorphous, since no diffraction lines were observed by a-XRD. The fraction of Zr contained in the calcium silicate phase decreases with increasing the temperature below the 20% in 1100 sample. The fraction of t-ZrO₂ increases reaching a maximum of 27-32% in the samples treated at intermediate temperatures (1000 and 1050 samples) and decreases to about 10% in the sample treated at 1100 °C. The m-ZrO₂ phase appears only after treating the sample at 1050 °C (43%) and its fraction increases rapidly raising the firing temperature till about 75% in 1100 sample.

XRD results appear fully coherent with a-XRD analysis: raising the firing temperature provokes the transition of Zr-containing phase from a Calcium Silicate environment toward tetragonal and monoclinic ZrO_2 phases. Notice that the XANES analysis allows probing all the phases containing Zr, either long range ordered either disordered (glass phase). This is different from a-XRD experiments, which allow probing only long range ordered phases. However the ratios between t- ZrO_2 to m- ZrO_2 phase fraction derived from the analysis of the XANES data are in good agreement with those obtained from a-XRD, this gives confidence on the results obtained.

3.2.2. EXAFS. The "ab-initio" quantitative refinement of the EXAFS spectra in this kind of samples, in which several Zr containing phases are presents with high degree of disorder, is a difficult task. However we exploited the previous knowledge coming from a-XRD and XANES techniques to constrain the analysis and improve the reliability of the EXAFS analysis.

The figure 7 shows the experimental k^2 weighted EXFAS data of the investigated samples. Details of the refinements are shown in figure 8. The EXAFS signals change weakly between AQ and 1000 samples, as already noticed from XANES data analysis. Raising the firing temperature (1050 and 1100 samples) provokes the appearance of high frequency structures in the EXAFS spectra point out the evolution toward a medium/long range ordered structure. The modulus of the Fourier transforms (FT) of the AQ and 1000 samples depict a disordered environment in which only a main nearest neighbour shell and a weak next neighbour shell are present. In the 1050 and 1100 samples the FT's dramatically change providing direct evidence of the crystallization progress as a function of firing temperature.

The quantitative analysis of the EXAFS data requires up to 6 partial contributions (figure 8) to reproduce the Zr atomic environment till about 3.7-4 Å. We found the

multiple scattering contributions negligible in this range (Li *et al.*, 1993) and only two bodies contributions were used (Filipponi & Di Cicco, 1995). For each shell we refined the multiplicity (coordination number, N), path length (coordination distance, R) and Debye Waller factor (variance, σ^2). We found N , R and σ^2 parameters of Zr-Si and Zr-Ca shell strongly correlated, thus, for sake of simplicity, the same distance and σ^2 were used for the two contributions, leaving free the two coordination numbers. Within this choice the N_{ZrSi} is similar to N_{ZrCa} for all the samples. The same $S_o^2 = 0.85$ was used analysing all the EXAFS spectra. We found the edge energy changing less than 0.6 eV among the various samples, then E_o was kept fixed for all the samples in the final refinements. The best fit parameters are resumed in table 3.

In the AQ sample the Zr is coordinated to 5-6 Oxygen neighbours located around 2.14Å. This Zr-O shell, however, appears heavily distorted and not Gaussian. This is due either to the intrinsic distortion of Zr-O environment in ZrO_2 polytypes (Table 4) either to the superimposition of different Zr local environments coherently with XRD and XANES results. In the AQ sample a double Zr-O shell improves the fitting but also produces large correlations among the fitting parameters. We found that, in this sample, a cumulant expansion (Filipponi & Di Cicco, 1995), including a skewness ($\beta \sim 1.5$) and a Kurtosis ($K \sim 0.05$) term improves the fitting while keeping reduced the correlation among the parameters without affecting the global structural results. In all the other samples the Zr-O nearest neighbour distribution is reproduced with two gaussian shells. The next neighbours shell is composed by a combination of Si and Ca neighbours located around 3.4Å in agreement with our previous results (Meneghini *et al.*, 1999). The Zr-Si/Ca coordination distance is similar to the Zr-Si/Ca distance expected, for example, in Gittinsite (see table 4) (Roelofsen-Ahl & Peterson, 1989) and this finding confirms that the Zr, in the as quenched glass, is embedded in a calcium silicate glassy phase. A Zr-Zr_I coordination shell is found around 3.55 Å. It appears

quite disordered ($\sigma^2 \sim .013 \text{\AA}^2$) and the distances is in between the Zr-Zr distances in m-ZrO₂ ($\sim 3.5 \text{\AA}$) and t-ZrO₂ ($\sim 3.65 \text{\AA}$).

In the 1000 °C sample the Zr-O nearest neighbour shell depicts a clear bimodal distribution characterized by two Gaussian contributions: the former being about 5 oxygen ions at about 2.16\AA while about 1 Zr-O bond is found around 2.35\AA . These distances being close to the first and second Zr-O distances expected in t-ZrO₂ structure (Table 4).

The coordination number and σ^2 of Zr-Si/Ca contributions change weakly, this pointing out a minor effect of thermal treatment on the Zr environment in the calcium silicate phase. The Zr-Zr next neighbour distribution is split in two contributions: the Zr-Zr_I at $\sim 3.5 \text{\AA}$ and the Zr-Zr_{II} at $\sim 3.65 \text{\AA}$ close to the first Zr-Zr shell in t-ZrO₂ polytype (table 4).

In the sample 1050 the first Zr-O shell does not change appreciably, but the Zr-O shell around 2.35\AA becomes more evident with increasing N (~ 2.5) and decreasing σ^2 ($\sim 6 \times 10^{-3} \text{\AA}^2$). The total Zr-O coordination number in 1050 sample is around 8 in agreement with a t-ZrO₂ structure (see table 4). The next neighbour distribution is characterized by three Zr-Zr contributions, the most intense (Zr-Zr_{II}) being located at 3.65\AA , similar to the first Zr-Zr coordination distance in t-ZrO₂ structure (table 4). The other two: Zr-Zr_I at $\sim 3.4 \text{\AA}$ and Zr-Zr_{III} $\sim 3.8 \text{\AA}$, should be associated to the increasing contributions from the m-ZrO₂ phase (see table 4).

In the 1100 sample the Zr-O nearest neighbour distances remain unchanged, while the coordination decreases slightly toward ~ 7 . The next neighbour distribution is characterized by the growth of Zr-Zr contributions associated to the monoclinic structure (Zr-Zr_I at 3.48\AA and Zr-Zr_{III} around 3.8\AA) while the Zr-Zr_{II} coordination number, associated to the t-ZrO₂ phase, decreases. All the Debye-Waller factors in 1100 sample decreases systematically, confirming the ordering of the structure around Zr

ions.

The results of the EXAFS analysis confirms that in the as quenched glass the Zr environment is mainly an amorphous calcium silicate phase. The thermal treatment provokes the segregation of Zr-rich phases in form of Zirconium oxides. The analysis of EXAFS data definitively confirms, coherently with a-XRD and XANES data, that Zr is present in at least three different phases: a Calcium Silicate and two ZrO_2 phases with monoclinic and tetragonal symmetry.

4. Conclusions

This work is intended to give a close insight about the role of Zr in the devitrification process of a CZS glass as a function of firing temperature, looking at the particular composition $(\text{CaO})_x(\text{ZrO}_2)_y(\text{SiO}_2)_z$ ($x \sim 0.4$, $y \sim 0.05$, $z \sim 0.55$). To this aim we combined complementary structural information coming from XRD and XAS techniques in order to give detailed picture of the Zr environment at short (atomic), medium and long range (crystallographic) scales.

The structure of the as quenched glass is essentially amorphous and the Zr is embedded in a calcium silicate glassy phase. The analysis of XAS data shows that the Zr ions are 6-coordinates in roughly octahedral configuration. This atomic environment closely resembles that of Gittinsite (Roelofsen-Ahl & Peterson, 1989) and comes in agreement with recent molecular dynamics simulations (Lancellotti *et al.*, 2002). The analysis of the XANES data suggests that a minor fraction of Zr could be in a Zr-rich environment, which local structure is close to that of t- ZrO_2 . Combined XRD and EXAFS results demonstrate that the devitrification process produces segregation of Zirconium oxide phases in form of t- ZrO_2 and m- ZrO_2 (Baddeleyite) and allows excluding the formation of other crystalline phases containing Zr.

The heat treatment at 1000 °C provokes the partial devitrification of the glass with

the formation of Wollastonite like phases. In the 1000 sample the effect of firing on the Zr environment is weak, however the analysis of a-XRD difference patterns put in evidence a t-ZrO₂ phase characterized by small/highly defective crystallites. The analysis of XAS data confirms the growth of Zr-oxide contribution and the decreasing of the fraction of Zr in the calcium silicate glassy phase.

The segregation of ZrO₂ oxide continues in the sample treated at 1050 °C. This sample displays a bimodal distribution of ZrO₂ particles characterized by smaller/poorly crystallized t-ZrO₂ particles and larger/better crystallized m-ZrO₂ crystallites. In 1100 sample the m-ZrO₂ phase fraction growth, while decreases the contribution of Zr in t-ZrO₂ and Calcium Silicate phases. It must be noticed that while the diffraction line width of m-ZrO₂ phase decreases raising the firing temperature between 1050 °C and to 1100 °C, the diffraction lines of m-ZrO₂ phase remain broader. This finding comes in agreement with the peculiar particle size dependence of ZrO₂ phase diagram that, for small particles, makes the t-ZrO₂ energetically more favourable than m-ZrO₂ (Garvie, 1965; Garvie, 1978).

Our structural results are interpreted as follow: thermal treatment provokes the segregation of Zr out from the Calcium Silicate glassy phase and the growth of Zirconium oxide particles. The observed ZrO₂ phase in the AQ samples (XANES) would provides the nucleation centers for t-ZrO₂ small crystallites firing the samples at 1000 °C. Raising the firing temperature provokes the growth ZrO₂ particles which stabilizes in the monoclinic structure.

Acknowledgements The excellent technical support of F. Campolungo (INFN-Frascati), V. Sciarra (INFN-Frascati) and V. Tullio (INFN-Frascati) and F. D'anca (INFM-OGG Grenoble), R. Weigel (BM29-ESRF) was greatly appreciated. The GILDA project is financed by the three Italian institutions: CNR, INFM and INFN.

References

- Amoros, J. L., Escardino, A., Orts, M. J. & Moreno, A. (1994). *Brit. Ceram. Trans.* **93**, 840–844.
- Ankudinov, A. L., Ravel, B., Rehr, J. J. & Conradson, S. D. (1998). *Phys. Rev. B*, **58**, 7565.
- Benfatto, M., Natoli, C. R., Bianconi, A., Garcia, J., Marcelli, A., Fanfoni, M. & Davoli, I. (1986). *Phys. Rev. B*, **34**, 5774–5781.
- Bianconi, A. (1988). chap. XANES Spectroscopy in X-Ray Absorption: EXAFS, SEXAFS, XANES., p. 573. John Wiley & Sons New York.
- Burger, K., Cox, D., Papoular, R., & Prandl, W. (1998). *J. Appl. Cryst.* **31**, 789–797.
- Canton, P., Fagherazzi, G., Frattini, R. & Riello, P. (1999). *J. Appl. Cryst.* **32**, 475–480.
- Dejus, R. J. & del Rio, M. S. (1996). *Rev. Sci. Instrum.* **9**, 67.
- Escardino, A., Moreno, A., Amoros, J. L., Gozalbo, A., Aparici, J. & Sanchez, L. F. (1996). *Cer. Acta*, **8**, 21–34.
- Filipponi, A. (1995). *J. Phys.: Condens. Matter*, **7**, 9343–9356.
- Filipponi, A., Borowski, M., Bowron, D. T., Ansell, S., De Panfilis, S., Di Cicco, A. & Itiè, J.-P. (2000). *Rev. Sci. Instr.* **71**, 2422–2432.
- Filipponi, A. & Di Cicco, A. (1995). *Phys. Rev. B*, **52**, 15135–15149.
- Filipponi, A., Di Cicco, A. & Natoli, C. R. (1995). *Phys. Rev. B*, **52**, 15122–15134.
- Filipponi, A. & DiCicco, A. (2000). *TASK QUARTERLY*, **4**, 575.
- Garvie, R. C. (1965). *J. Phys. Chem.* **69**, 1238–1243.
- Garvie, R. C. (1978). *J. Phys. Chem.* **82**, 218.
- Hammersley, A. P., Svensson, S. O. & Thomson, A. (1994). *Nucl. Instrum. Methods Phys. Res. A*, **346**, 312321.
- Hann, R. E. & Al (1985). *J. Amer. Ceram. Soc.* **68C**, 285–286.
- James, F. (1994). *MINUIT: Function MINimization and Error Analysis. Reference Manual - V 94.1*. Program Library D506, CERN.
- Kordyuk, R. A. & Gul’ko, N. V. (1962). *Dokl. Chem. Tech.* **142**, 6–10.
- Lancellotti, I., Leonelli, C., Montorsi, M., Pellacani, G. C., Siligardi, C. & Meneghini, C. (2002). *Phys. Chem. Glasses*, **43C**, 108.
- Larsen, A. C. & Von Dreele, R. B. (2000). *GSAS General Structure Analysis System*. Los Alamos National Laboratory, Los Alamos, New Mexico.
- Lee, P. A., H., P., Citrin, Eisenberger, P. & Kincaid, B. M. (1981). *Rev. Mod. Phys.* **53**, 769–806.
- Lee, P. A. & Pendry, J. B. (1975). *Phys. Rev. B*, **11**, 2795–2811.
- Li, P., Chen, I.-W. & Penner-Hahn, J. E. (1993). *Phys. Rev. B*, **48**, 10063–10073.
- Mac Millan, P. (1964). *Glass Ceramics*. London. Academic Press.
- Materlik, G., Sparks, C. J. & Fisher, J. (1994). *Resonant Anomalous X-ray scattering theory and applications*. Elsevier Science, Amsterdam.
- Matsumoto, K., Sawamoto, T., Koide, S. & Hokoku, A. K. (1954). *Asahi Garasu Kenkyu Hokoku*, **4**, 8–13.
- Meneghini, C., Artioli, G., Norby, P., Balerna, A., Gualtieri, A. & Mobilio, S. (2001). *J. of Synchrotron Rad.* **8**, 1162–1166.
- Meneghini, C., Gualtieri, A. & Siligardi, C. (1999). *J. Appl. Cryst.* **32**, 1090–1099.
- Neilson, G. F. (1972). *Advances in Nucleation and Crystallization in Glasses.*, vol. 5. Am. Ceram. Soc. Spec. Publ.
- Pascarelli, S., Boscherini, F., D’Acapito, F., Hrdy, J., Meneghini, C. & Mobilio, S. (1996). *J. Synchrotron Rad.* **3**, 147–155.
- Roelofsen-Ahl, J. N. & Peterson, R. C. (1989). *Canad. Mineral.* **27**, 703–708.
- Strnad, Z. (1986). *Glass ceramic materials*. Elsevier.

- Vogel, W. (1994). *Glass Chemistry*. Berlin, Springer.
- Warren, B. E. (1990). *X-ray diffraction*. Dover Publications, INC., New York.
- Warren, B. E. & Averbach, B. L. (1950). *J. Appl. phys.* **21**, 595.
- Warren, B. E. & Averbach, B. L. (1952). *J. Appl. phys.* **23**, 497.
- Weinberg, M. C. (1993). *Nucleation and crystallization in liquids and glasses*. The American Ceramic Society.
- Willilamson, G. K. & Hall, W. H. (1953). *Acta Metall.* **1**, 22.
- Wilson, A. J. C. (1962). *Proc. Phys. Soc.* **80**, 286.
- Wright, A. F. & Lehmann, M. S. (1981). *J. Sol. Stat. Chem.* **36**, 371–380.

Table 1. *Crystallographic structure of Zr-containing long range ordered phases: A=t-ZrO₂, B=m-ZrO₂. Statistical uncertainties on the last digit are reported in parenthesis. The maximum size of crystallites (D) for each phase has been estimated using the Sherrer formula (see text). In the last column the volume fraction of the two phases is reported. Lattice parameters for t-ZrO₂ (ref. (Canton et al., 1999)) and m-ZrO₂ (ref. (Hann & Al, 1985)) are reposted for shake of comparison.*

	Ph.	a Å	b Å	c Å	β deg.	D nm	Vol%
1000	A	3.63(1)		5.20(1)		8(1)	100
1050	A	3.63(1)		5.23(2)		15(1)	59(6)
	B	5.16(2)	5.26(3)	5.36(3)	98.9(2)	20(1)	41(6)
1100	A	3.63(2)		5.23(2)		16(2)	19(4)
	B	5.18(9)	5.24(3)	5.34(2)	99.0(2)	40(2)	81(4)
t-ZrO ₂	A	3.629		5.197			
m-ZrO ₂	B	5.151	5.203	5.315	99.2		

Table 2. *Experimental XANES data were fitted with a linear combination of theoretical signals calculated for crystalline Zr oxide polytypes: t-ZrO₂, m-ZrO₂ and Gittinsite (Si₂CaZrO₇). The statistical uncertainty on the last digit is reported in parenthesis.*

	t-ZrO ₂ %	m-ZrO ₂ %	Si ₂ CaZrO ₇ %
AQ	20(4)	-	80(4)
1000	27(4)	-	73(4)
1050	32(5)	43(6)	25(4)
1100	9(2)	73(7)	18(3)

Table 3. *EXAFS results. The statistical uncertainties on the last digit are reported in parenthesis.*

Pair	N	R (Å)	$\sigma^2 \times 10^3 \text{Å}^2$		N	R (Å)	$\sigma^2 \times 10^3 \text{Å}^2$
	RT				1050		
Zr-O _I	5.5(3)	2.14(2)	5.6(6)		5.5(5)	2.16(1)	6.4(6)
Zr-O _{II}	-	-	-		2.3(2)	2.35(2)	7.0(7)
Zr-Si/Ca	0.9(2)/0.8(2)	3.43(2)	6.5(5)		2.6(2)/2.3(2)	3.40(2)	5.6(6)
Zr-Zr _I	-	-	-		0.9(2)	3.42(2)	9.5(6)
Zr-Zr _{II}	1.8(2)	3.55(2)	13(2)		4.4(3)	3.65(2)	6.5(6)
Zr-Zr _{III}	-	-	-		2.0(4)	3.78(3)	15.3(5)
	1000				1100		
Zr-O _I	5.3(3)	2.16(1)	6.2(6)		5.0(4)	2.17(1)	6.2(6)
Zr-O _{II}	1.3(2)	2.35(2)	12(2)		2.2(2)	2.35(2)	6.0(6)
Zr-Si/Ca	1.3(2)/1.0(2)	3.40(2)	6.6(5)		2.4(2)/2.0(2)	3.40(2)	3.1(2)
Zr-Zr _I	1.4	3.48(2)	6.5(7)		2.7(2)	3.48(3)	6.1(3)
Zr-Zr _{II}	2.0	3.64(2)	10.(1)		3.6(2)	3.65(2)	4.2(2)
Zr-Zr _{III}	-	-	-		3.0(4)	3.77(4)	6.3(5)

Table 4. *Zr coordination distances in crystalline polytypes used for XAS data analysis.*

	t-ZrO ₂	m-ZrO ₂	Si ₂ CaZrO ₇
ZrO	2.11×4 2.38×4	2.07×2, 2.14 2.17×2 2.26, 2.32	2.07×4 2.15×2
ZrZr	3.65×12	3.36, 3.49 × 5 3.62, 3.93×2 4.0×2	
ZrSi			3.4×4 3.55×2
ZrCa			3.4, 3.55×2

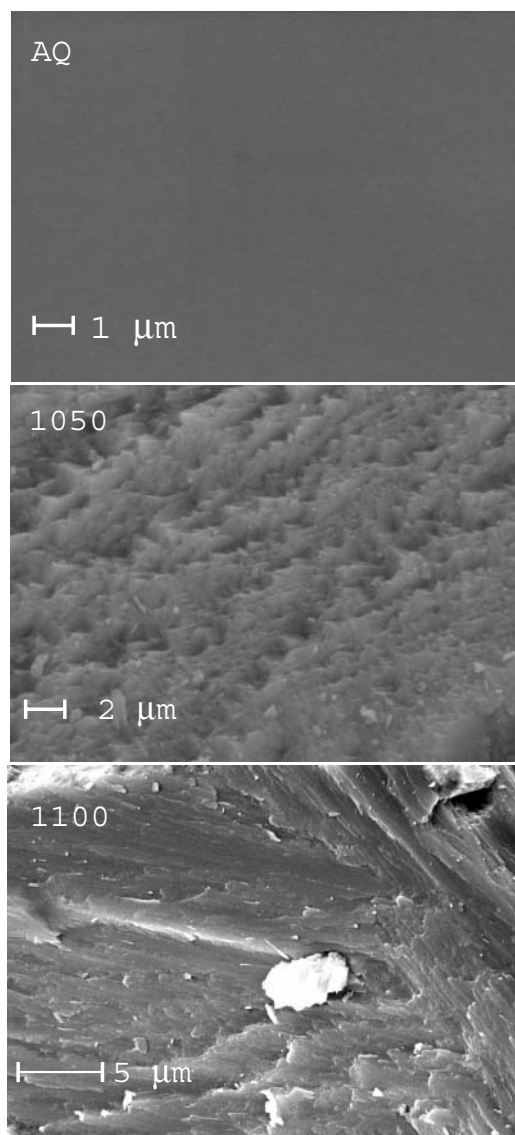


Fig. 1. SEM images of our $(\text{CaO})_{0.4}(\text{ZrO}_2)_{0.05}(\text{SiO}_2)_{0.55}$ samples. The AQ sample (top panel) depicts homogeneous glassy structure. Fired samples (1050 and 1100 respectively) present poly-crystalline habit, typical of glass ceramics. In the glass treated at 1000 °C in backscattering geometry. The white grain clearly visible in 1100 sample (lower panel) must be a Zr-rich particle (backscattering image).

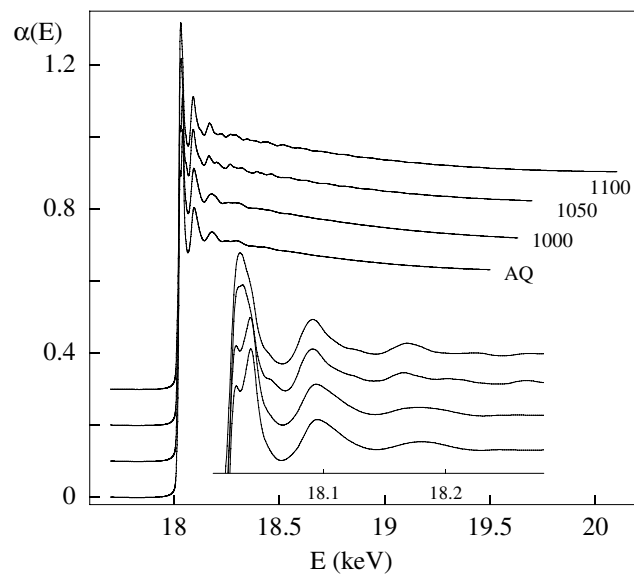


Fig. 2. Raw XAS data of the four samples investigated.

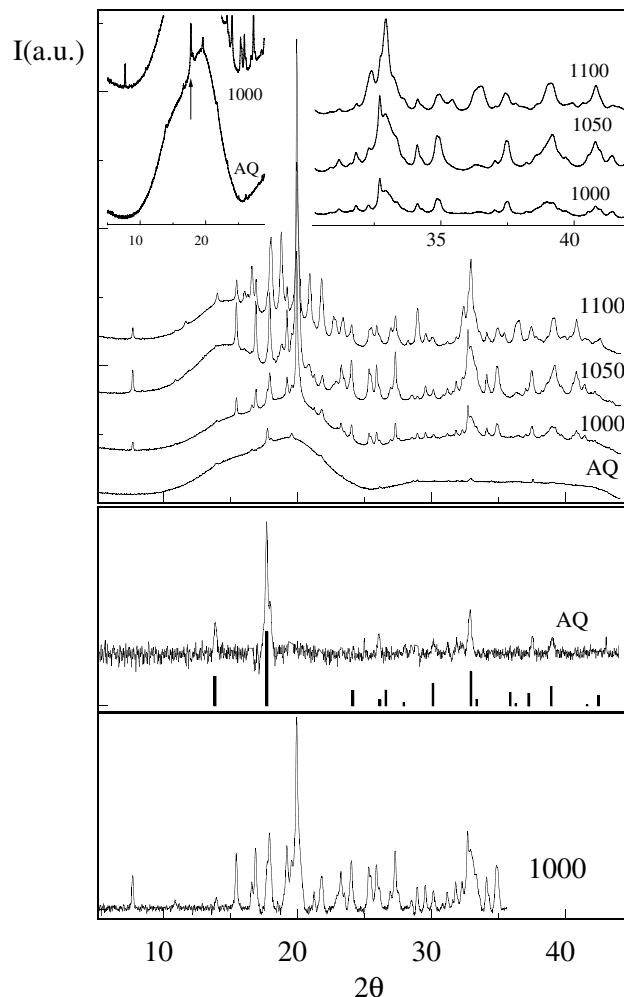


Fig. 3. The upper panel reports the raw XRD patterns for the samples investigated collected with $\lambda = 1.045 \text{ \AA}$. In the insert are shown fine details of the diffraction patterns demonstrating the high quality of the data. In particular the weak diffraction peaks visible in the AQ sample pattern must be ascribed to quartz phase particles. The lower panels plot the $\sqrt{I_{exp} - I_{bck}}$ where I_{exp} are the experimental data and I_{bck} is the background modelled with a polynomial spline. Calculated diffraction lines pattern for quartz structure are shown, shifted for clarity. In the lower panel the $\sqrt{I_{exp} - I_{bck}}$ for 1000 sample is shown. The main features suggest a Wollastonite-like phase.

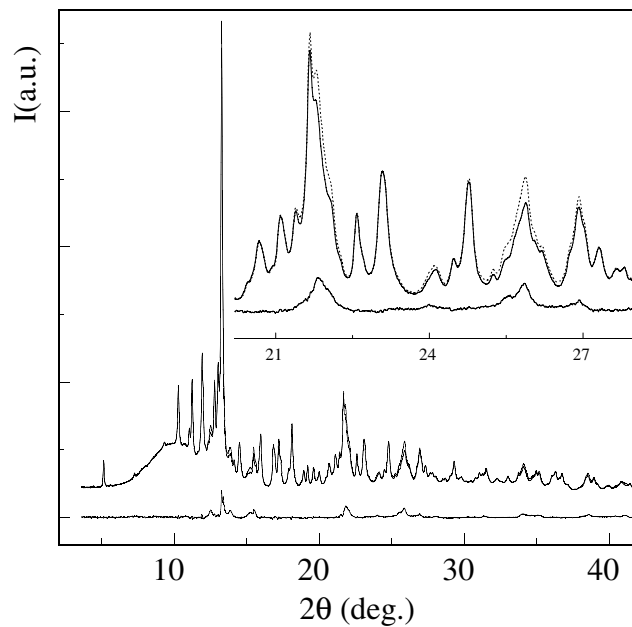


Fig. 4. Anomalous diffraction on 1050°C sample: XRD patterns collected at 17000 eV (dashed line) and at 17990 eV (full line) together the difference pattern. The difference pattern only retains features concerning to the Zr containing phases. In the insert the subtraction procedure is highlighted.

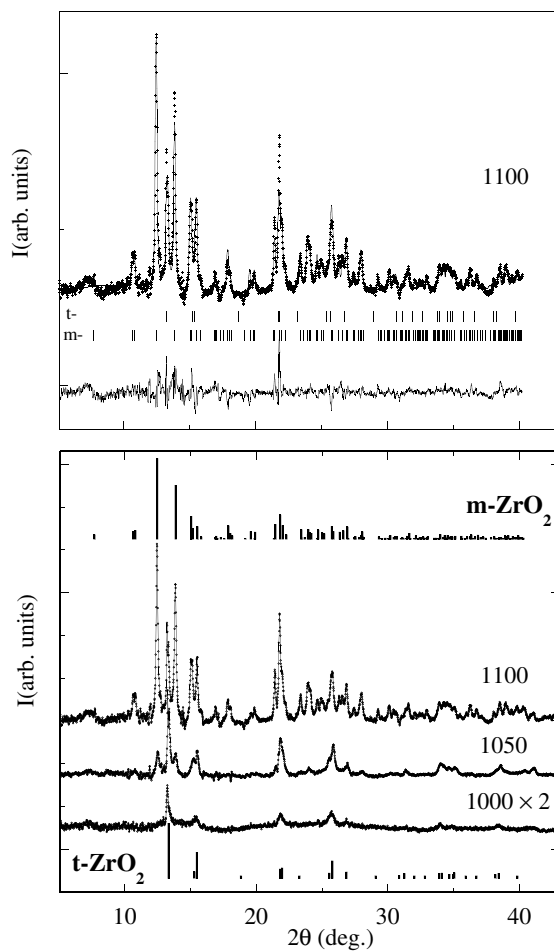


Fig. 5. **Upper panel:** example of Rietveld profile refinement on 1100 difference pattern: the experimental data (crosses) and fit (full line) are shown. The residual is reported shifted below for clarity. In the **middle panel** the markers signal the positions of diffraction lines for tetrahedral (t-) and monoclinic (m-) structures. **Lower panel:** Difference curves for 1000, 1050 and 1100 samples are shown, shifted for clarity. On the top and bottom of the lower panel the calculated patterns for m-ZrO₂ t-ZrO₂ polytypes are shown for sake of comparison.

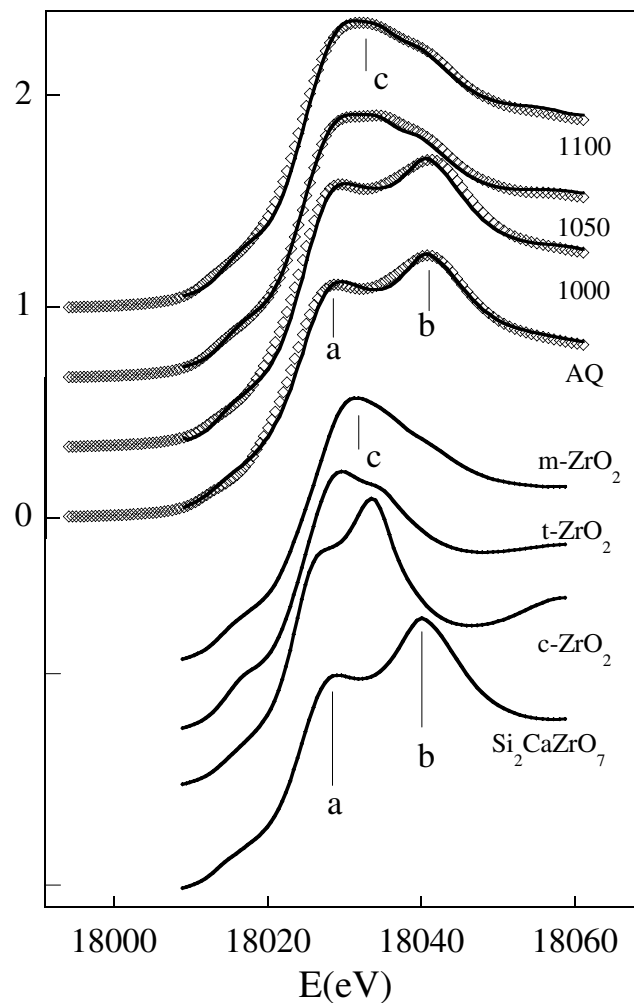


Fig. 6. The upper data represent the experimental XAS data (diamonds) in the XANES region and fit (full lines) obtained as linear combinations of simulated signals (see text). The lower curves are the simulated XANES for Zr polytypes. The curves are vertically shifted for clarity.

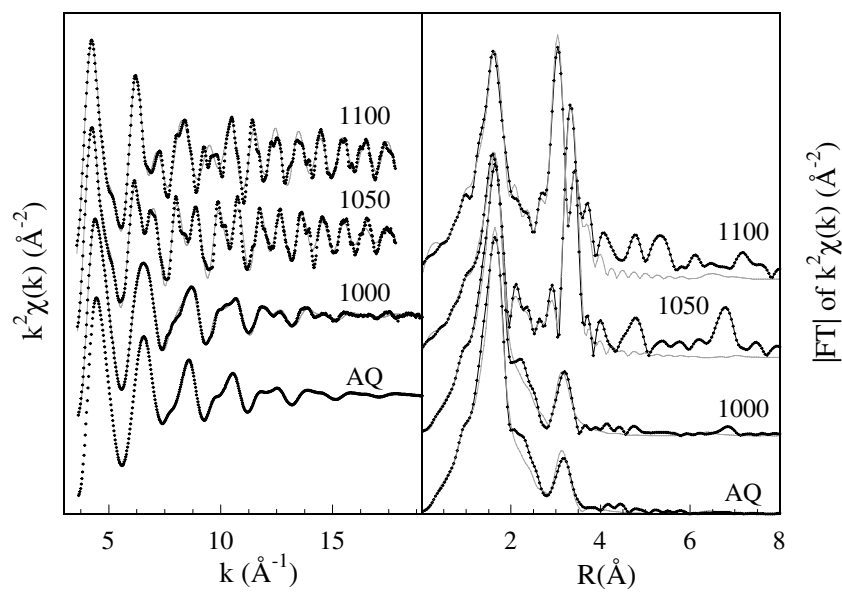


Fig. 7. The experimental k^2 weighted EXAFS data (left panel, dots) and the modulus of their Fourier Transform (right panel, dots) are shown. The k^2 weighted theoretical $\chi(k)$'s (left panel, full lines) and their Fourier Transforms (right panel, full lines) are shown.

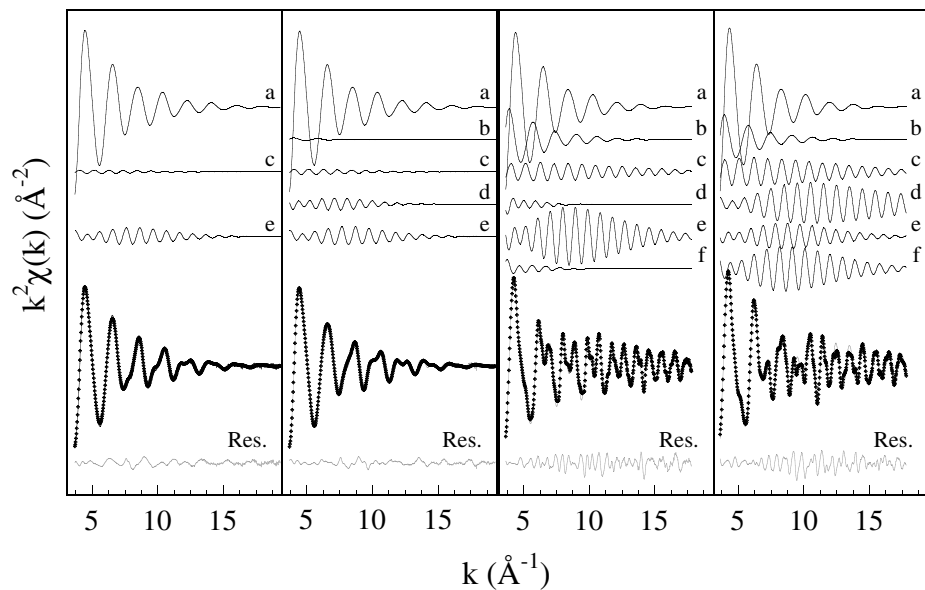


Fig. 8. Experimental EXAFS data (dots) and best fit (gray lines). The partial contributions are shown shifted upward for clarity: $a=\text{ZrO}_I$, $b=\text{ZrO}_{II}$, $c=\text{ZrSi}+\text{ZrCa}$, $d=\text{ZrZr}_I$, $e=\text{ZrZr}_{II}$, $f=\text{ZrZr}_{III}$. The residuals (best fit minus experimental) are reported, shifted downward for clarity. The quite large residual observed in 1050 and 1100 samples is mainly determined by high frequency structural signals ($R > 4\text{\AA}$) not considered in the fitting (see text).

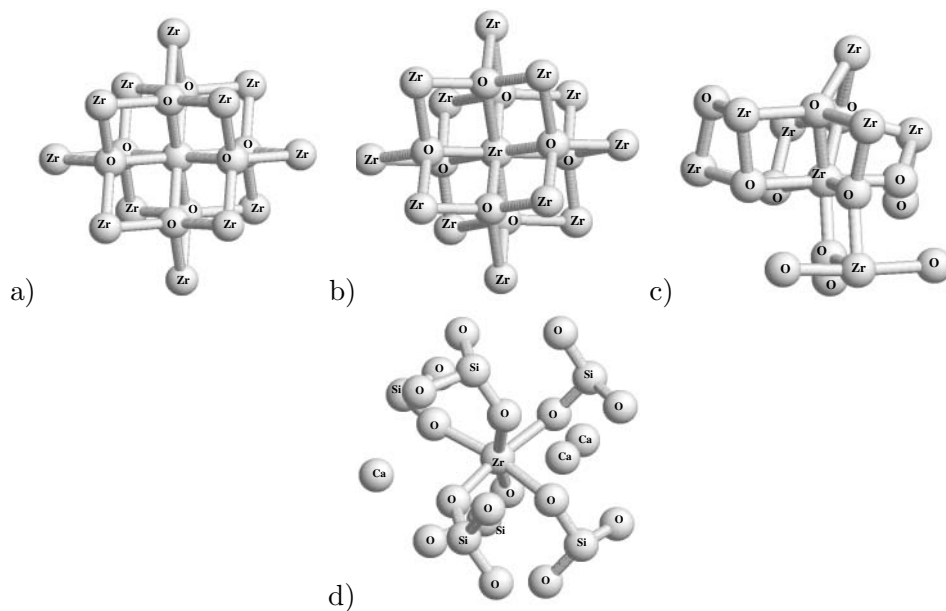


Fig. 9. Local atomic structure around Zr in model polytypes used for XANES simulation: c-ZrO₂ (a), t-ZrO₂ (b), m-ZrO₂ (c), Si₂CaZrO₇ (d).

Synopsis

The effect of devitrification process on the Zr-containing phases in a CaO-ZrO₂-SiO₂ glass-ceramic has been studied combining x-ray anomalous diffraction and x-ray absorption spectroscopy techniques.
